LoRaMirror: Illuminating Blind Spots in Urban LPWAN with Reflective Smart Surfaces

Songfan Li, *Member, IEEE,* Yanbo Zhang, Jansen Christian Liando, Li Lu, *Member, IEEE,* Mo Li, *Fellow, IEEE*

***Abstract*—The deployment of low-power wide-area networks (LPWAN) in urban environments faces a critical challenge with signal blockage caused by dense obstacles like buildings, resulting in *blind spots* where end nodes have difficulty reaching the gateway. This paper proposes LoRaMirror, a reflective smart surface design, to essentially eliminate these blind spots and improve overall communication in urban LoRaWAN. LoRaMirror is different from existing smart surface designs, as it addresses unprecedented challenges posed by LPWAN's unique application scenario of extremely long communication distances, extremely low data transmission rates, and extremely wide coverage. LoRaMirror is prototyped with a 16-antenna multi-layer array and the experimental results show significant performance gains in real world practice.**

***Index Terms*—Reconfigurable Intelligent Surface, Metasurface, LoRa, IoT, Blind Spots.**

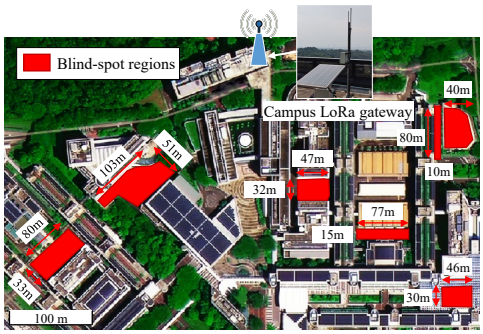

Fig. 1. Distributed and small blind spots (average profile 70m×30m) within the LoRa gateway coverage.

I. Introduction

Practical deployment of low-power wide-area networks (LPWAN) such as LoRaWAN [1], [2] and NB-IoT [3] in urban environments often encounters a significant challenge in the form of signal blockage caused by buildings and other dense structures [4]. These obstacles dramatically attenuate the signal strength, creating widely distributed *blind spots* where sensor nodes struggle to reach their gateway due to poor signal-to-noise ratio (SNR) conditions. As shown in Fig. 1, a survey of blind-spot regions around a 50-acre area covered by one LoRa gateway in our campus testbed reveals the extent of the problem. The uplink packet receive rates (PRR) of those blind-spot nodes are below 10% on average, even when configured with the maximum transmission power (20 dBm) and spreading factor (SF12).

Simply deploying additional gateways to cover numerous small blind spots is not a feasible solution, as complex urban landscapes result in an inefficient increase in coverage rates [5], along with high deployment and maintenance costs. An alternative solution could be to deploy a relay node near each blind-spot region, which receives data packets from end nodes and forwards them to the gateway [6], [7]. Decode-and-forward relaying, however, requires additional bandwidth for repeated packet forwarding, which reduces spectrum efficiency. Moreover, relay nodes suffer from high energy consumption because of the continuous monitoring of the channel and relaying of data, which is not practical for battery-powered IoT applications.

Existing efforts to improve LoRa communication links, such as Choir [8], Falcon [9], and NELoRa [10], may also be employed to mitigate the blind-spot problem. For example, Choir aims to extend the uplink range by letting multiple nodes transmit coherent data, Falcon allows a blind-spot node to deliver data by selectively interfering with ongoing transmissions of a nearby LoRa node to the gateway, and NELoRa uses a neural-enhanced demodulation method to improve the SNR sensitivity of gateways. Other works that coordinate distributed gateways to improve signal decodings [11], [12], correct bit errors [13], or improve SNR by selecting optimal carrier frequency [14], have also been proposed. However, these approaches cannot address the root cause of blind spots, $i.e.$, the signal attenuation caused by obstacles, and thus have limited performance.

This paper aims to tackle the blind-spot problem in an essential way – by utilizing reflective smart surfaces to let LoRa signal bypass obstacles. A reflective smart surface does not radiate electromagnetic (EM) signals but passively reflects the incident signals, creating a reflection link between the end node and gateway. Unlike non-configurable EM reflectors that provide a fixed reflection link [15]–[17], smart surfaces can control the phases of reflected signals from an antenna array and steer a beam of strengthened signal towards the gateway, making a better fit to urban LPWAN applications which are subject to dynamic channels and uncertainty over long-range signal propagation.

This paper introduces LoRaMirror, a hardware and software

Songfan Li and Mo Li are with the Department of Computer Science and Engineering, The Hong Kong University of Science and Technology. Emails:{lisongfan, lim}@ust.hk. *Corresponding author: Mo Li*

Yanbo Zhang and Jansen Christian Liando are with the College of Computing and Data Science, Nanyang Technological University (NTU).

Li Lu is with the School of Computer Science and Engineering, University of Electronic Science and Technology of China (UESTC).

This work is supported in part by Ministry of Education Singapore MOE AcRF Tier 2 MOE-T2EP20220-0004, in part by the Start-up Fund of HKUST under grant R9899, in part by Hong Kong GRF under grant 16204224, and in part by the National Natural Science Foundation of China under Grant U21A20462.

co-designed reflective smart surface to eliminate blind spots and enhance overall communication quality for urban LoRaWAN. While most existing works implement smart surfaces in small scale wireless systems, $e.g.$, Wi-Fi or mmWave which typically have sub-hundred meter communication range [18]–[23], LoRaMirror faces unprecedented challenges that stem from the unique features of LPWAN application scenario, in its extremely long communication distances, extremely low data rates, and extremely wide coverage of numerous end nodes. The design of LoRaMirror has to address the following three unique challenges.

Challenge-1: LPWAN communication at kilometer-scale significantly weakens the efficacy of the reflective link. Unlike most existing applications where the smart surfaces are deployed right next to either the transmitter (Tx) or receiver (Rx) to mitigate reflection loss [18], [19], [21], [24], LoRaMirror for bypassing obstacles has to be placed away from the Tx/Rx ends, which significantly weakens the reflection power. Using a large scale of antennas to improve signal reflection is infeasible in the 915 MHz LoRa frequency band due to the significant size of the antennas and the extensive overhead required for beamforming search. To address this challenge, LoRaMirror co-designs high-gain antennas and a beamforming scheme, incorporating a Yagi-Uda based antenna structure that enhances signal reflection while minimizing the number of antennas required. To guarantee the high-gain property in LPWAN settings, an EM polarization-agnostic antenna design is proposed, which maintains power efficiency when reflecting signals that are polarized in various directions from arbitrarily placed LoRa end nodes. With a co-designed phase shifter, each LoRaMirror antenna is independently phase controlled when reflecting the incident EM waves and converts arbitrary linearly polarized signals to circularly polarized signals in backscattering.

Challenge-2: Extremely low data rate of LPWAN challenges the search for the best beamforming configurations of smart surfaces. Due to its modulation designed for extremely low SNR conditions and low power consumption, LoRa communication is subject to low data rates, $i.e.$, three to six orders of magnitude lower than what Wi-Fi and mmWave offer. Existing beam search methods of smart surfaces in other wireless systems may incur prohibitive communication overheads when applied to LoRaWAN. For example, RFocus [20] built for Wi-Fi sends thousands of probing packets to search the optimal phase configuration which only takes one second with its Wi-Fi setting, but may take hours when sending those probes in LoRa. While LAIA [18] and ScatterMIMO [19] use fewer probing packets, they require precise channel estimation which is ill-suited to extremely weak ($i.e.$, < -120 dBm) signals from LPWAN blind spots. LoRaMirror addresses this challenge in two steps: (i) A novel blind beamforming method is proposed to reduce the beam search space. Different from existing blind beamforming [21], [22], a more complicated beam search space needs to optimize due to the lack of precise knowledge of relative positions of LoRa nodes and gateways over the kilometer-scale reach of communication. (ii) By utilizing the chirp modulation of the LoRa physical layer, a symbol-level beam search scheme is proposed, which assesses varied beamforming configurations in symbols, instead of packets, to reduce the overhead in both transmission time and energy consumption.

Challenge-3: The application requirement of widely covering numerous end nodes appeals for new beamforming modes to provide breath. While beamforming with high-gain antennas can effectively concentrate signal power for higher SNR gain in depth, it faces an essential limit to its breath, $i.e.$, the beam width of the reflected signal becomes narrow which is not always preferred for the following two reasons: (i) The long communication distance makes LoRa Rx sensitive to directional errors of the narrow beam - especially during the blind beam search when the reflected probing signal may not reach the gateway at all. (ii) Narrow beams are not suitable for the widespread coverage of numerous LoRa end nodes during downlink one-to-many transmissions from the gateway. To address these limitations, LoRaMirror exploits unique phase configuration patterns to scatter the rays of the reflected signal over a wider range of directions, regardless of the incident signal direction. Such a "scattering mode" provides wider beam coverage with a trade-off on SNR gains. LoRaMirror scattering is essentially different from existing multi-beam method [21], [25] which creates multiple beams towards different directions. The multi-beam solution requires knowledge of the precise locations of blind-spot nodes to formulate phase configurations and is limited in its beam numbers which is not realistic in LoRaWAN application.

For proof of concept, a LoRaMirror prototype has been built with 4×4 antenna elements, at a size of 0.8×0.8 m^2. The prototype achieves a signal reflection gain of 25.6 dB, which can be further enhanced without increasing the number of antennas due to the extendable antenna structure. The prototype is capable of working collaboratively with commercial LoRa nodes and gateways. Comprehensive experiments are conducted to evaluate the performance of the prototype with two LoRa testbeds on campus. The results suggest that even when the LoRaMirror is deployed ∼1 kilometer away from the gateway, it can still extend the coverage by up to 70 m of signal penetration into the blind-spot region. It can provide up to 17.5 dB SNR gains to a blind-spot node with its original received SNR below -22 dB, which translates to over 90% improvement in packet reception ratio (PRR). With better SNR conditions LoRaMirror may support 5.7× uplink throughput improvement. Two application scenarios of deploying LoRaMirror are studied, (i) to eliminate blind spots and (ii) to enhance general communication quality over a wide region including non-blind spots. To the best of our knowledge, LoRaMirror is the first attempt in designing a practical smart surface for LPWAN system and application.

II. Related Work

Smart surfaces and antenna designs: Smart surfaces [26]–[29] and meta-surfaces [25], [30]–[32] are gaining attention due to their programmable capability to manipulate radio environments. Recent efforts have been developing novel surfaces for diverse wireless systems including Wi-Fi [18], [19], 6G [22], [26], satellite [33] and acoustic sensing [34]. Specific

antenna designs have been proposed for different purposes such as area-efficiency [21], polarization rotation [35], almost-360° FOV [22], [25], dual frequency band [36] and frequency-tunable soft antenna [37]. Different from the above works, LoRaMirror primarily addresses the unique challenges from the extremely long communication distances, extremely low data rates, and extremely wide coverage of LPWAN.

Linear-to-circular polarization conversion: Existing polarization conversion techniques can be classified into two methods. The first method [38], [39] is to design a polarization conversion circuit to receive a signal from a linearly polarized antenna and transmit it through a circular polarized antenna. Such a method cannot be used in LoRaMirror as the incident signal polarization is unknown. Alternatively, customized antenna designs [40]–[43] have been proposed to transform the signal polarization, which however is ill-suited to LoRaMirror due to the collision against the Yagi-Uda structure for high-gain beamforming. Different from the above works, this paper accomplishes the linear-to-circular conversion with the Yagi-Uda structure and a co-designed phase shifter is proposed to achieve simultaneous phase control for both beamforming and polarization conversion.

Blind beamforming: Existing beamforming models for smart surfaces often consider simplified scenarios where the smart surface sit next to the Tx with a known incident angle. RFLens [21] presents a beamforming model built upon a near-field condition, where the incident angle and the distance between RFLens and its gateway are thus assumed known. Similar assumption is made in mmWall [22], [25], where the incident angle is fixed as precise locations of the gateway and the smart surface are known. In the case of LoRaMirror, however, the precise relative directions between LoRaMirror and the LoRa gateway or end nodes are difficult to obtain due to the kilometer-scale communication as well as the arbitrary deployment of end nodes.

Non-configurable reflectors: Prior work [15]–[17] use pre-fabricated meta-surfaces or reflectors with beamforming capability for mmWave coverage expansion. For kilometer-scale communication, however, non-configurable meta-surfaces are challenging to predetermine the fixed beam accurately and cannot re-steer their beams when the communication link is blocked or varies with the environment dynamics.

Amplify-and-forward relays: Recent work explores extending the coverage of wireless networks using signal relays. MoVR [44] designs active mmWave reflectors to relay communications for reliable indoor virtual reality. LAVA [24] employs a multi-directional amplifier array to relay communication for optimized indoor coverage. Those works are ill-suited to LoRaMirror due to the high power consumption and exhaustive use of the wireless channel bandwidth.

In addition to above system works, Xiaoyu *et al.* [45] simulate a smart surface assisted LoRa network and Zhaokun *et al.* [46] theoretically analyze the anti-interference performance of using a smart surface in LoRa systems. But, they do not concern any system challenges of adopting the smart surfaces in practical LPWAN.

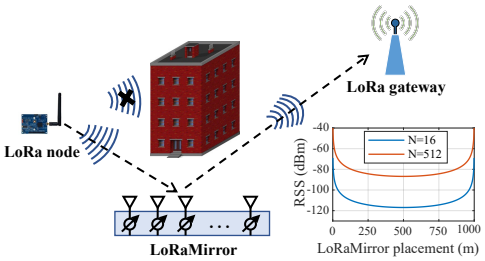

Fig. 2. LoRaMirror setting for a bind spot. N is the number of LoRaMirror antennas.

III. LoRaMirror Antenna Design

A. Long Distance Reflection Loss

Existing studies [18], [19], [21], [24] used to place smart surfaces close to either the Tx or Rx of a communication link to mitigate path loss. When extending LPWAN coverage, however, LoRaMirror has to be positioned with distance from both Tx and Rx, to bypass major urban obstacles and cover an area of blind spots as large as possible. To understand this challenge, we consider LoRa communication at a blind spot where the communication between a LoRa node (Tx) and a gateway (Rx) is blocked as shown in Fig. 2. A LoRaMirror surface with N antennas deployed in between Tx and Rx provides a reflective link to bypass the obstacles. On the reflective link, the received signal power at Rx side can be described according to the Friis transmission formula [19], [47].

$$P_R = N^2 P_T \frac{G_T G_a^2 G_R \lambda^4}{(16\pi^2 d_1 d_2)^2} \tag{1}$$

where P_T is the transmission power from Tx, G_T, G_R are the antenna gains of the Tx and Rx, and G_a represents the antenna gain of LoRaMirror, d_1 denotes the distance between the Rx and LoRaMirror, and d_2 is the distance between LoRaMirror and Tx. λ is the wavelength of radio frequency.

In Fig. 2, the received signal strength (RSS) is visualized for a 1 km Tx/Rx separation when LoRaMirror uses $N = 16$ commonly used dipole antennas with 2.1 dB gain, considering 20 dBm transmission power from the Tx node. We note that the RSS decreases from above -80 dBm at the Tx or Rx side, quickly dropping to below -100 dBm when the smart surface is placed 40 meters away from the Tx or Rx. If we want to increase the RSS value to above -80 dBm, more than 500 antennas will be needed. Operating this many antennas at the 915 MHz LoRa frequency band is almost impossible for the large antenna size and significant overhead needed for beamform search.

In this paper, we investigate improving the antenna gain to elevate the RSS value. From Equation (1), we observe that the antenna gain of LoRaMirror (G_a) and the number of antennas (N) equally contribute to the RSS improvement. For example, by increasing the antenna gain to 14 dB, we can approach the RSS curve of $N = 512$ by using only 32 antennas.

B. High Gain Yagi-Uda Antenna

Most high-gain antennas, however, are ill-suited for LoRaMirror, as they necessitate a large planar surface to effec-

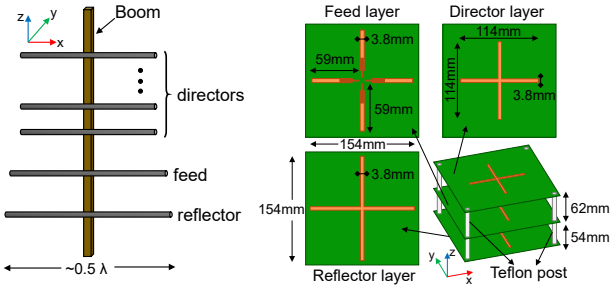

Fig. 3. (a) The conventional Yagi-Uda antenna structure. (b) LoRaMirror antenna structure (with one director layer). The antenna substrate measures 20 cm by 20 cm with a thickness of 0.16 cm. The z axis is the maximum radiation direction.

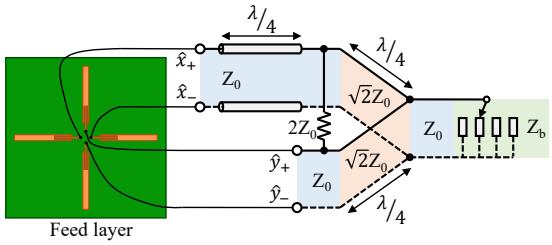

Fig. 4. Polarization agnostic backscatter circuit with co-designed phase shifter for both beamforming and polarization conversion. $\hat{x}_+$ and $\hat{x}_-$ are connected to the x-direction antenna, while $\hat{y}_+$ and $\hat{y}_-$ are for the y-direction antenna. Z_b denotes the controllable impedance to generate phase shifts.

tively capture electromagnetic waves. For example, parabolic antennas typically provide a gain of 30-50 dB, but will occupy an area from $100\lambda^2$ to $10000\lambda^2$. While horn antennas and corner reflectors have a smaller form factor, a typical area of $10\lambda^2$ to $50\lambda^2$ is still needed.

In this paper, we design our antenna based on the Yagi-Uda structure that features only $0.25\lambda^2$ of the plane area and provides a high gain of up to 20 dB. Fig. 3(a) illustrates the structure of the conventional Yagi-Uda antenna which consists of a feed dipole antenna, a reflector and a number of directors. The feed dipole is connected to a radio chain for signal reception and transmission, whereas the reflector and directors are parasitic components that have no electrical connection with the feed dipole. All components are attached to a boom and together form a frequency resonator that produces a high gain towards the beam direction. The achieved gain is higher when more directors are included.

While the conventional Yagi-Uda antenna offers an ideal structure for constructing high-gain smart surfaces, the polarization mismatch in IoT may significantly undermine its gain. The Yagi-Uda antenna, as well as the typical antennas employed by IoT end devices, are linearly polarized. Significant polarization mismatch loss (theoretically up to ∞ dB) can occur when these antennas are misaligned [35], particularly when end device antennas are oriented perpendicularly to the smart surface antenna. Unfortunately, pre-aligning them is impractical, given that IoT devices are deployed with a variety of conditions, such as walls, grounds, slopes, and altitudes, which lead to differently oriented polarization.

To address the polarization mismatch, we adopt a crossed Yagi-Uda antenna structure as depicted in Fig. 3(b). The feed layer comprises two orthogonal antennas in order to harness the full power from EM waves of arbitrary polarization angles. Each antenna includes an inset feed method to control their impedance to match with the backscatter circuit for signal phase control (details in section III-C). Similarly, parasitic components including the reflector and directors are in cross shapes for resonating with the feed layer. All layers are combined via four Teflon posts between each layer. The posts are fully extendable and flexible so the gain of the LoRaMirror antenna can be manually configured by adding a desired number of director layers [48], [49]. Our simulation with the high-frequency structure simulator (HFSS) shows that the antenna gain is 7.1 dB when one director is used, and can achieve 10.2 dB when additional two directors are included.

C. Polarization Agnostic Backscatter

Although the cross design in the LoRaMirror antenna can harvest signal power from arbitrary polarization angles, how to constructively join the power from the two antennas when backscattering is non-trivial. In particular, this has to be co-designed with the phase shifter that is required to configure each LoRaMirror antenna for beamforming.

We devise a polarization agnostic backscatter circuit that directly converts the linearly polarized signals to circular polarization, and simultaneously controls the phase of the reflected signal for beamforming purpose. A circular polarized antenna can be used at the gateway to receive the reflected signal without any polarization loss, or if a linear polarized antenna is used at the most 3 dB loss is incurred. Fig. 4 plots the backscatter circuit design which is the co-designed phase shifter for both beamforming phase control and linear-to-circular polarization conversion. Specifically, the signal backscatter process can be divided into two steps: signal capture and re-radiation. A linearly polarized signal first is captured by the two antenna components $\hat{x}$ and $\hat{y}$ respectively, which will then be constructively combined by the circuit. In this design, the backscatter phase control is imposed when the signal is received before re-radiation. Finally, the phased signal will be split into two branches with $\frac{\pi}{2}$ phase difference and flow back to the antennas for re-radiation with circular polarization.

The circuit design principle can be described mathematically as follows. Consider a linearly polarized E-field signal traveling in the z direction, the E-field vector will be:

$$\vec{\mathbf{E}} = E_0 e^{j(\omega t - kz)} \begin{pmatrix} \cos\theta_p \\ \sin\theta_p \end{pmatrix} \tag{2}$$

E_0 is the amplitude of the E-field and θ_p is an arbitrary polarization angle of the incident signal. $e^{j(\omega t-kz)}$ denotes that the E-field is traveling in the z direction, in which ω is the angular frequency and k is the wave number.

When the E-field is captured by the LoRaMirror antenna, the received signals can be expressed as $E_0 e^{j\omega t}\cos\theta_p$ and $E_0 e^{j\omega t}\sin\theta_p$ on x-direction and y-direction antennas, respectively. Further, as a $\frac{\pi}{2}$ phase difference provided by the $\lambda/4$

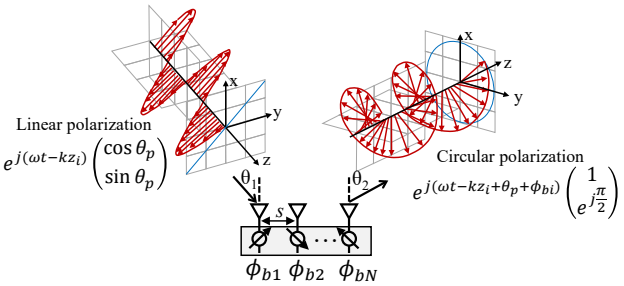

Fig. 5. Geometry of the polarization agnostic backscatter for beamforming. ϕ_{bi} is the independent phase control of the i^{th} antenna.

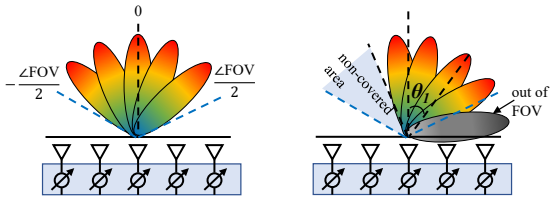

(a) $\theta_1 = 0°$ (b) $\theta_1 \neq 0°$

Fig. 6. The beam steering angle with the same coded book. (a) When $\theta_1 = 0°$, the beam steering angle covers the whole FOV. (b) When $\theta_1 \neq 0°$, the same coded book can only cover a part of the FOV. The beam out of the FOV is invalid.

transmission line is applied to the two signals, they can be constructively combined as:

$$E_0 e^{j\omega t}\cos\theta_p + E_0 e^{j\omega t}\sin\theta_p \cdot e^{j\frac{\pi}{2}} = E_0 e^{j(\omega t+\theta_p)} \tag{3}$$

Equation (3) demonstrates that the phase shifter can convert any linearly polarized signals to a initial phase of the received signal with no polarization mismatch. At this stage, we apply the beamforming phase shift to the received signal by controlling the RF backscatter switch to select an impedance Z_b that generates a desired phase shift ϕ_b, obtaining $E_0 e^{j(\omega t+\theta_p+\phi_b)}$.

Then, the phased signal will be re-radiated via the phase shifter that equally splits the signal power into x-direction and y-direction antennas and applies a $\frac{\pi}{2}$ phase difference between them. The re-radiated (backscattered) E-field signal can be denoted by:

$$\vec{\mathbf{E}} = \frac{E_0}{2} e^{j(\omega t-kz+\theta_p+\phi_b)}\begin{pmatrix}1\\ e^{j\frac{\pi}{2}}\end{pmatrix} \tag{4}$$

Equation (4) suggests that the backscattered signal turns a circularly polarized signal with a polarization spin of ω. Fig. 5 illustrates the process of the linear-to-circular backscatter. In the next section, we will introduce the beamforming model with LoRaMirror antennas.

LoRaMirror differs from a recent effort LLAMA [35] that achieves linear-to-linear polarization rotation to address the polarization mismatch. Note that finding the best rotation to match the polarization in [35] may introduce non-trivial iterative search overheads especially for LoRa devices which are purposed for years of lifespan.

IV. Fast Beamforming

A. Beamforming Model

Fig. 5 also plots the geometry of the beamforming model, where s denotes the spacing between antennas. θ_1 is the incident spatial angle and θ_2 is the reflection spatial angle. LoRaMirror placement is assumed meeting the far field conditions [50], as it is often placed distance away from both the LoRa end node and gateway so the incident EM signals arrive at LoRaMirror in form of a plane wave. From the geometry, the initial phase on the i^{th} antenna can be determined according to the propagation distance $z_i = z_{i-1} + s\cdot\sin\theta_1$. The reflection beam pattern with N antenna elements can be formulated as below. For convenience, we omit the phase shift θ_p that is irrelevant to the beamforming.

$$F_A = \sum_{n=1}^{N} e^{j(n-1)[ks(\sin\theta_1-\sin\theta_2)+\Delta\Phi]}\begin{pmatrix}1\\ e^{j\frac{\pi}{2}}\end{pmatrix} \tag{5}$$

where $\Delta\Phi$ denotes the phase shift between adjacent antenna elements. Owing to the polarization agnostic backscatter circuit, the applied $\Delta\Phi$ for beamforming is same on both x and y directions, thus not corrupting the circular polarization.

To beam the reflected signal towards the direction of θ_2, the phase shift $\Delta\Phi$ shall follow.

$$\Delta\Phi = ks(\sin\theta_2 - \sin\theta_1) \tag{6}$$

The reflection beam pattern can be generalized to the case of the planar array by considering the joint effect of beamforming in azimuth and elevation planes as below.

$$F_{A(\text{azi})} = \sum_{n=1}^{N} e^{j(n-1)[ks(\sin\theta_1-\sin\theta_2)(\cos\phi_1-\cos\phi_2)+\Delta\Phi_{\text{azi}}]}\begin{pmatrix}1\\ e^{j\frac{\pi}{2}}\end{pmatrix}$$

$$F_{A(\text{ele})} = \sum_{m=1}^{M} e^{j(m-1)[ks(\sin\theta_1-\sin\theta_2)(\sin\phi_1-\sin\phi_2)+\Delta\Phi_{\text{ele}}]}\begin{pmatrix}1\\ e^{j\frac{\pi}{2}}\end{pmatrix}$$

where N and M denote the number of antennas along azimuth and elevation planes, respectively. ϕ_1 and ϕ_2 denote the incident and reflection angle in elevation plane, and θ_1 and θ_2 are for azimuth plane. The phase shifts $\Delta\Phi_{\text{azi}}$ and $\Delta\Phi_{\text{ele}}$ are independent, corresponding to the two dimensional steering of the reflect beam.

B. Optimizing the Beam Search Space

According to Equation (6), as k and s are fixed physical factors, the required phase shift $\Delta\Phi$ of beamforming can be derived when both θ_1 and θ_2 are known. Most existing blind beamforming methods for smart surfaces [21], [22] suppose that θ_1 (or θ_2) has been fixed (as the smart surface is deployed near by the Tx or Rx), and search for θ_2 (or θ_1) to prepare a code book of $\Delta\Phi$ for blind beam search. Precisely estimating θ_1 or θ_2, however, is often impossible in LoRaWAN setting due to its kilometer-scale distance of communication and unknown locations of distributed end nodes. A strawman solution would thus engage an iterative process to search both θ_1 and θ_2, leading to a search space of $\mathcal{O}(N^2)$ where N denotes the number of antennas of the smart surface.

LoRaMirror mitigates this problem according to the observation that a code book for some fixed θ_1 can be exploited to steer the beam for an arbitrary θ_1. Equation (6) can be transformed to $\theta_2 = \arcsin(\frac{\Delta\Phi}{ks} + \sin\theta_1)$, in which the phase shift $\Delta\Phi$ provides a relative angle $\Delta\theta$ of beam steering to the incident angle θ_1. Given that both θ_1 and θ_2 for reflective smart surfaces are within $(-\frac{\pi}{2}, \frac{\pi}{2})$, this is a monotonically

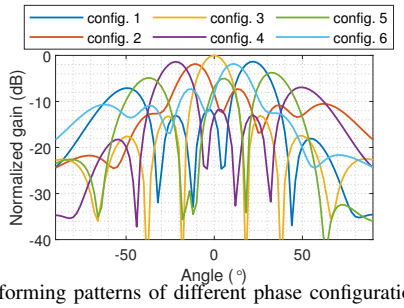

Fig. 7. Beamforming patterns of different phase configurations.

increasing function for arbitrary θ_1. Therefore, LoRaMirror can prepare a simple $\{\Delta\Phi\}$ code book to steer the reflection beam, by assuming a fixed incident angle, for convenience, say $\theta_1 = 0°$. The same code book can be used to steer the beam for an arbitrary θ_1.

The code book designed for $\theta_1 = 0°$, however, is unable to cover the whole field of view (FOV) of LoRaMirror when $\theta_1 \neq 0°$. Fig. 6 illustrates such an issue with its spatial coverage. A non-covered area may exist using the same coded book, where the gateway may unfortunately locate. To tackle such a problem, the search area of the beam steering is increased to cover the entire FOV for any arbitrary θ_1. We denote the beam steering angle of the reflected signal by $[-\frac{\angle\text{FOV}}{2}+\theta_1, \frac{\angle\text{FOV}}{2}+\theta_1]$ for an arbitrary θ_1, where $\angle$FOV is the FOV angle and $\theta_1 \in [-\frac{\angle\text{FOV}}{2}, \frac{\angle\text{FOV}}{2}]$. Therefore, the beam steering angle can be completed by designing a code book that consider a doubled search space with $[-\angle\text{FOV}, \angle\text{FOV}]$. Such a way adds little redundancy of the search space but avoids the cumbersome iterative search process.

Our method has the search space of $\mathcal{O}(N)$, whereas the iterative search space is $\mathcal{O}(N^2)$. The search space for spatial coverage is determined by the FOV range divided by the beam width of the reflected signal. The FOV range is decided by the element factor [51] and thus does not vary over the number of antenna elements as well as the granularity in phase control. The search space is thus naturally related to the beam width of the reflected signal. In particular, the beam width in radians of uniform planar arrays is as follows [29], [52]:

$$\theta_{BW} = \frac{0.886\lambda}{Ns\cos\theta_2} \tag{7}$$

Although the beam width may vary over different reflection angles, we consider the worst case where $\cos\theta_2 = 1$, leading to the minimal beam width and thus the upper bound of the search space, which is linearly related to the number of antennas:

$$\mathcal{O}(\frac{Ns}{0.886\lambda}) \sim \mathcal{O}(N)$$

LoRaMirror solution searches in a doubled FOV range, and thus has a search space with the same linear complexity $\mathcal{O}(N)$. The iterative process will search over both θ_1 and θ_2 in a FOV range, which leads to a search space of $\mathcal{O}(N^2)$.

Fig. 7 plots the reflection beamforming pattern (in azimuth plane) of LoRaMirror prototype as simulated by the HFSS ($\Delta\Phi = \{0, \frac{\pi}{2}, -\frac{\pi}{2}, \pi, -\pi, \frac{3\pi}{2}\}$). It is worth to note that four of the six configurations, *i.e.* config.1 ($\Delta\Phi = -\frac{\pi}{2}$) and 3-5 ($\Delta\Phi = 0, \frac{\pi}{2}, \pi$, respectively), are adequate to cover the FOV of $[-50°, 50°]$, while config.2 ($\Delta\Phi = \frac{3\pi}{2}$) and config.6 ($\Delta\Phi = -\pi$) may be employed to complete the coverage when $\theta_1 \neq 0°$. As a result, LoRaMirror solution has a total number of $6 \times 6 = 36$ configurations in the beam search. If adopting the iterative search process a number of 16 configurations in azimuth plane, and a total number of 256 configurations in both azimuth and elevation planes need to be examined. The gap will be much wider if more antennas are employed.

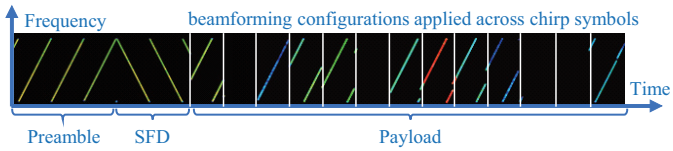

Fig. 8. Symbol-level beam search. LoRaMirror exploits the payload symbols to carry beamforming configurations.

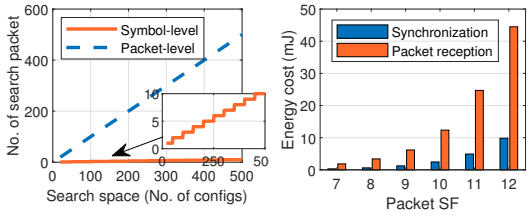

(a) (b)

Fig. 9. (a) Compare symbol-level and packet-level search efficiency in terms of probing packets needed. (b) Contrast the energy consumption of self-synchronization with receiving a LoRa packet.

C. Symbol-level Beam Search

Although the spatial beam search design significantly reduces the search space, the overhead of conventional packet based channel probing where each beam configuration is tested with one specific packet transmission is prohibitive due to the time and energy cost of each LoRa transmission. LoRaMirror thus devises a symbol-level beam searching scheme. As illustrated in Fig. 8, the chirp symbols contained in the payload of the LoRa transmission are exploited for beam searching. Each specific beamforming configuration is applied to one or several chirp symbols and one packet may carry symbols enumerating all possible configurations. The gateway demodulates the LoRa packet and uses per symbol SNR measurements to determine the optimal beamforming configuration. At the end of the beam search stage, a feedback packet containing the best configuration is applied to provide an optimal reflection link for each node.

To achieve such a scheme, it is necessary for LoRaMirror to punctually detect the arrival of every LoRa symbol. LoRaMirror needs to align the probed beamforming phase configuration to each LoRa symbol duration. If the beam searching process is misaligned with the symbols, different symbol SNR measurement is obtained, which further leads to the sub-optimal or even wrong selection of the beamforming configuration.

The LoRaMirror surface employs a self-synchronization scheme to align with the incoming LoRa symbols without the need of exchanging control messages with the Tx (which is infeasible in its time and energy cost). The standard LoRa

Channel Activity Detection (CAD) is used to detect the preamble symbols of the probing packet. In essence, the CAD function computes the correlation between the received symbol and a pre-defined up-chirp reference [53]. CAD is invoked periodically during the beam searching stage and captures the preambles until the start frame delimiter (SFD) to achieve the synchronization. Such an operation, however, is subject to CAD processing latency which leads to overlap of processing the preambles and handling the payload symbols.

LoRaMirror addresses this issue by exploiting the fact that the CAD processing delay is a fixed constant factor for a specified spreading factor (SF). We measure the processing delay of standard SF configurations with commercial LoRa chipset SX127X [54] and derive the CAD processing time p (normalized to the symbol length of the corresponding SF), i.e., 0.91 for SF7, 0.8 for SF8, 0.75 for SF9, 0.76 for SF10, 0.8 for SF11, and 0.85 for SF12. LoRaMirror customizes the preamble length to accommodate the delay, denoted by $N_s = 10 \times (1+p)$ symbols. For SF8 and SF11, the preamble length can be set as 18 chirps to align the CAD reading and the preamble timing. For other SF configurations, a residual time offset exists, e.g., 0.1 symbol length for SF7 and 0.5 symbol length for SF9, which can be compensated by applying the corresponding delay before triggering the beam search.

Appendix A provides more design details that take into account unsynchronized clock shifts between LoRa nodes and the LoRaMirror surface, as well as the measurement of symbol SNR in such scenarios.

Fig. 9(a) evaluates the efficiency of the proposed symbol-level beam search scheme with comparison to the packet based scheme where each beamforming configuration is carried by an entire packet. The result shows over 50× improvement on its time efficiency. Fig. 9(b) gives the energy profile of the self-synchronization which shows it consumes lower energy than a single LoRa packet reception does. This is because the synchronization is only needed during preamble detection and the CAD operation requires much less computation than packet reception.

V. Scattering

Although beamforming with high-gain antennas provides the highest SNR gain to each individual blind-spot node, it is subject to its limited coverage. Concentrating the signal power towards one direction naturally forms a beam of narrow width compared to the incident signal. The proposed high gain antenna design further narrows the beam width and aggravates the limited coverage. This section therefore proposes the scattering mode, a special phase configuration pattern for LoRaMirror to increase its angle coverage.

A. Scattering Mode

To achieve scattering, the key idea is to group the antenna elements, and let them disperse the signal towards different directions. For a linear array, the phase difference $\Delta\Phi$ of adjoining elements increases from the antennas in the center to those on the sides. Specifically, $\Delta\Phi = 0$ is configured for a group of antennas at the center and $\Delta\Phi = \alpha$ for the groups beside the center, where α is the atomic phase shift that provides smooth ray dispersing. The phase shift increases towards antenna groups on the sides of the array, *i.e.*, $\{2\alpha, 3\alpha, ...\}$, and can be indicated as $(i-1)\alpha$ for the i^{th} group from the center. The LoRaMirror array factor in the scattering mode is thus formulated as below.

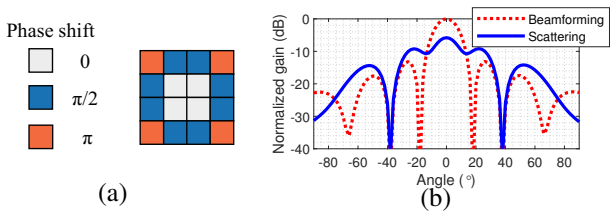

Fig. 10. (a) Scattering mode phase setting of the LoRaMirror prototype. (b) Beam width of the scattering mode (2.7× wider than the beamforming mode).

$$F_A^s = \sum_{n=1}^{N} e^{j(n-1)[ks(\sin\theta_1 - \sin\theta_2) + \Delta\Phi(n)]} \begin{pmatrix} 1 \\ e^{j\frac{\pi}{2}} \end{pmatrix}$$

where the phase shift $\Delta\Phi(n)$ varies across different groups:

$$\Delta\Phi(n) = \begin{cases} |n - \frac{N}{2}| \cdot \alpha & \text{N is even} \\ (\frac{N-1}{2} - n) \cdot \alpha & \text{N is odd and } n \le \frac{N-1}{2} \\ (n - \frac{N+1}{2}) \cdot \alpha & \text{N is odd and } n \ge \frac{N+1}{2} \end{cases} \quad (8)$$

The scattering pattern can be further generalized to the case of the planar array by jointly considering both azimuth and elevation planes.

$$F_{A(\text{azi})}^s = \sum_{n=1}^{N} e^{j(n-1)[ks(\sin\theta_1 - \sin\theta_2)(\cos\phi_1 - \cos\phi_2) + \Delta\Phi_{\text{azi}}(n)]} \begin{pmatrix} 1 \\ e^{j\frac{\pi}{2}} \end{pmatrix}$$

$$F_{A(\text{ele})}^s = \sum_{m=1}^{M} e^{j(m-1)[ks(\sin\theta_1 - \sin\theta_2)(\sin\phi_1 - \sin\phi_2) + \Delta\Phi_{\text{ele}}(m)]} \begin{pmatrix} 1 \\ e^{j\frac{\pi}{2}} \end{pmatrix}$$

Similar to the linear array, $\Delta\Phi_{\text{azi}}(n)$ and $\Delta\Phi_{\text{ele}}(m)$ increase from the center antenna group towards those around the edges in both azimuth and elevation planes, respectively, and can be calculated in the same way in Equation (8). The phase configurations on the diagonals can be filled with α phase shift to their horizontal and vertical values. Fig. 10(a) depicts the scattering configuration of the LoRaMirror prototype with a 4×4 array, and Fig. 10(b) depicts the HFSS simulated beam pattern of the scattering mode with comparison to the beamforming mode (towards 0°). We see that while the maximum gain of the main lobe is reduced by ∼5.8 dB, the scattering mode joins the main lobe and its first side lobes and generates a wider beam. For our prototype, the scattering mode improves the beam width to 76°, 2.7× wider than the 28° beam width in its beamforming mode. Next section discusses two usage cases of the scattering mode.

B. Usage Cases

Beam search from cold start. As illustrated in Fig. 11, LoRaMirror surface employs the probing packet in searching the best configurations for unknown blind-spot nodes, so the scattering mode can be used to improve coverage of probing packets for gateway detection. Specifically, the packet has two parts: (1) *Preamble*. During the preamble LoRaMirror stays in

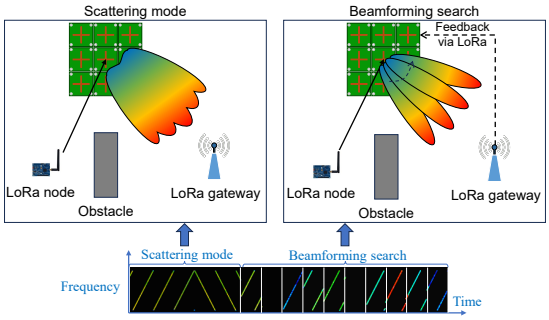

Fig. 11. Use of scattering mode and beamforming search for cold start.

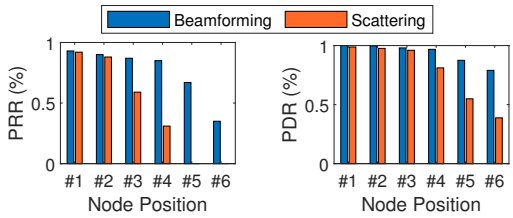

Fig. 12. The measured PRR and PDR of the beamforming mode and scattering mode of the six nodes.

scattering mode, achieving broad reflections so the gateway can detect the LoRa frame. (2) *Payload*. For the payload chirps LoRaMirror cycles through candidate beamforming configurations, one per chirp. The gateway measures the RSSI of each chirp and—by selecting the strongest—determines the beam pattern that yields the highest link margin.

The probing packet detection for most cases can be ensured as the preamble symbols are better detected than payload symbols — the preamble symbols do not carry data and thus contain contiguous chirps which are more easily detectable when CAD is performed [53]. Fig. 12 illustrates the distinction between packet detection (PDR) and packet decoding (PRR). Six nodes are placed in various locations (across different number of walls and buildings) to emulate a range of channel conditions. The packet reception ratio (PRR) measures the percentage of successfully received and decoded packet, which indeed shows that due to lower SNR gain the scattering mode cannot keep up with the best beamforming. However, the packet detection ratio (PDR) measures the percentage of packets captured by preamble detection (not necessarily decoded) which suggests that the scattering mode can provide comparable performance for each probing packet detection, but effectively reduce the number of probes for its wider coverage. As long as the probing packets are captured, the symbol-level beam search can be facilitated by assessing the SNR of different payload symbols (without the need of decoding them).

LoRaMirror's receive (Rx) chain is activated only during the cold-start phase: it powers up to synchronize with the node's probing packet and to capture the gateway's beamforming feedback. After cold start, the Rx chain remains off almost continuously, minimizing power consumption.

At the end of the cold-start phase, the gateway transmits a feedback packet to both the LoRaMirror surface and the node, specifying the chosen beamforming pattern and the assigned uplink time slot. In its subsequent uplink frames, the node raises a flag to confirm successful reception of this configuration.

Improving downlink throughput. In the scattering mode, the wider beam width covers a wider range of blind-spot nodes at a time, so it is ideal to support downlink traffic when the gateway broadcasts to end nodes in a one-to-many way (which is typical for IoT applications [55]–[57]). The main advantages of using the beamforming mode or the scattering mode for general data traffics are summarized as follows.

Beamforming mode provides the highest SNR improvement to individual end node and thus can be applied to extend the LoRa reachability and improve uplink throughput. Multiple nodes can be supported through time-division multiple access (TDMA) scheme.

Scattering mode provides wide coverage at a time and thus can be applied to best support one-to-many downlink traffic. When using the scattering mode LoRaMirror is transparent to the end nodes as no coordination is needed between the end nodes, the gateway, and the reflection surface.

VI. Implementation

Hardware prototype. LoRaMirror is prototyped with assembled antenna elements and phase control boards as depicted in Fig. 13(a). The current prototype includes one director layer (7.1 db gain) to evaluate the gain of LoRaMirror at the least. Each antenna element connects to a phase shifter that finally is connected to the phase control board. The phase shifter provides 2-bit phase shift ($i.e.$, 0, $\frac{\pi}{2}$, π, $\frac{3\pi}{2}$) using the RF switch BGS14MPA9. Fig. 13(b) depicts the logical connection between the functional blocks. One phase control board can operate up to six adjacent antenna elements. All phase control boards are controlled by a central controller. A feedback Rx chain is implemented with an SX1276, and is enabled only at the end of the beam search stage when the gateway sends a feedback packet to the LoRaMirror surface to explicitly indicate the best beamforming configuration for an end node.

The gateway side is primarily based on a commercial off-the-shelf (COTS) LoRa gateway that incorporates the LoRa concentrator IC880A. As the COTS gateway does not provide symbol-level SNR measurement, the prototype employs USRP N210 only for chirp-level SNR assessment (which we believe can be easily integrated in future hardware).

Power profile. LoRaMirror can be implemented with low power consumption for the following reasons. First, LoRaMirror uses passive antenna elements that do not consume power once configured with certain beamforming settings. The RF switch BGS14MPA9 consumes power of 3.6 μW in idle and 108 μW in operating, which only requires 0.6 μJ to set 36 phase configurations across 16 antennas in its beam search. Second, given the low data rates, the symbol duration of LoRa is in milliseconds ($\sim$1 ms for SF7 and $\sim$32 ms for SF12). Consequently, ultra-low power MCUs operating at just a few MHz, such as MSP430FR5969 that consumes $\sim$200 μW in active mode [58], are sufficient for GPIO control and central processing. Third, the Rx chain on the surface is only exploited during the beam search and stays off most of the time. Overall,

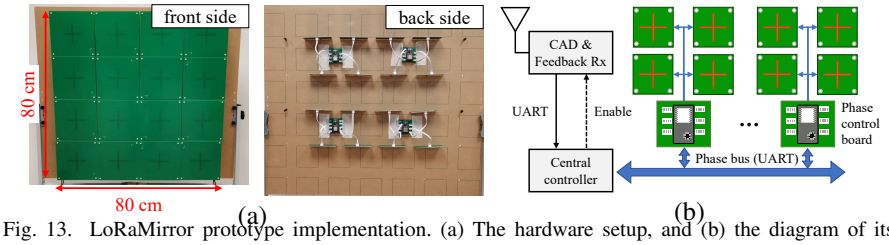

Fig. 13. LoRaMirror prototype implementation. (a) The hardware setup, and (b) the diagram of its functional blocks.

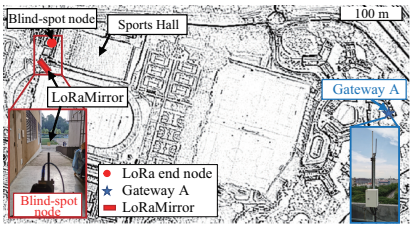

Fig. 14. Testbed 1 for the quantitative evaluation.

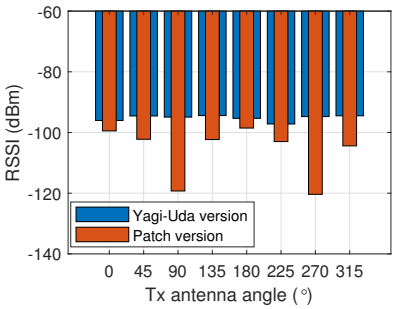

Fig. 15. LoRaMirror antenna based on the Yagi-Uda structure (7.1 dB gain) and the previous version of vertically polarized patch antennas (4 dB gain).

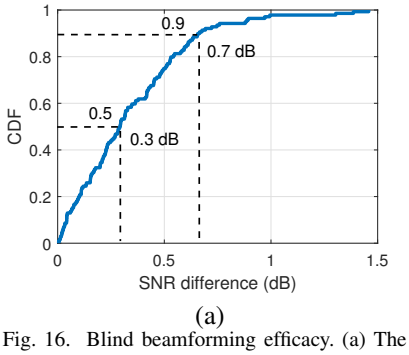

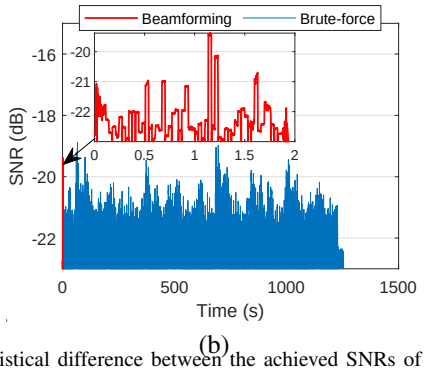

Fig. 16. Blind beamforming efficacy. (a) The statistical difference between the achieved SNRs of LoRaMirror beam search and brute-force search. (b) Comparison of the search time of the two search schemes.

LoRaMirror can achieve μW-level average power profile in typical use, which results in 3-5 years of expected battery lifespan.

VII. Evaluation

A. Experimental Setting

We conduct experimental study with two testbeds, *i.e.*, (i) one as depicted in Fig. 14 for its longer distance (near 1 kilometer) between the gateway and the blind spots, and (ii) the other as depicted in Fig. 1 for its various landscapes and regions of blind spots in real world LPWAN applications.

LoRaMirror placement. The surface is deployed outside the blind-spot area with a minimal LOS distance to the gateway. The LoRa end nodes are deployed in the blind-spot area with varied distances to the LoRaMirror (see Section VII-D in detail). Both LoRaMirror and the nodes are positioned 1 m above ground level to ensure proper signal propagation.

In this section we present the experimental results from the first testbed (Fig. 14). The direct path from the LoRa end node to the gateway is blocked by the sports hall with an average signal attenuation of ∼57 dB. The average SNR of end node transmissions in the shaded area is below -22 dB when a maximum Tx power of 20 dBm is used. Such a setting allows wide range control of parameters and quantitative assessment of performance gain from LoRaMirror for varied communication conditions.

B. Polarization

We evaluate the received signal power (RSSI) at the gateway with different antenna orientations at the Tx end device. In the experiment, LoRaMirror is configured to the best beamforming setting. We experiment with two versions of antenna design – the current LoRaMirror design with the proposed Yagi-Uda antenna as described in Section III (with 7.1 dB gain), while the other is a previous effort using vertically polarized patch antennas with 4 dB gain (see Appendix B for more details). The Tx end device uses a linear dipole antenna. We rotate the Tx antenna clockwise and record the RSSI at the gateway with different Tx antenna orientations.

Fig. 15 compares the RSSI results of the two antenna designs. As expected, the current LoRaMirror antenna can efficiently reflect linearly polarized signals with arbitrary angles. While the current LoRaMirror antenna gain is 3.1 dB higher than the previous patch version, we see significant RSSI improvement, especially when the Tx antenna is badly aligned with the patch antenna, e.g., up to 25.6 dB gain when they are perpendicular (90° and 270°). Overall, the average improvement of the current LoRaMirror design is 11 dB over the previous patch antenna design. It is worth noting that the gateway in the experiment uses a vertically polarized antenna for variable control. If a circular polarized antenna is used at the gateway, the improvement will be even higher (minimum 9.2 dB and 17 dB on average). The RSSI improvement can be further improved by adding more directors to the current LoRaMirror antenna. With the HFSS simulation, the overall improvement can be further increased by 4.2 dB and 9.4 dB when three or four director layers are used, respectively.

C. Beamforming Efficacy

LoRaMirror adopts blind beamforming that achieves a near optimal solution to support blind-spot nodes. To verify this, we conduct experiments to compare the achieved SNR performance from the proposed beam search scheme with the brute-force search that enumerates all possible phase configurations

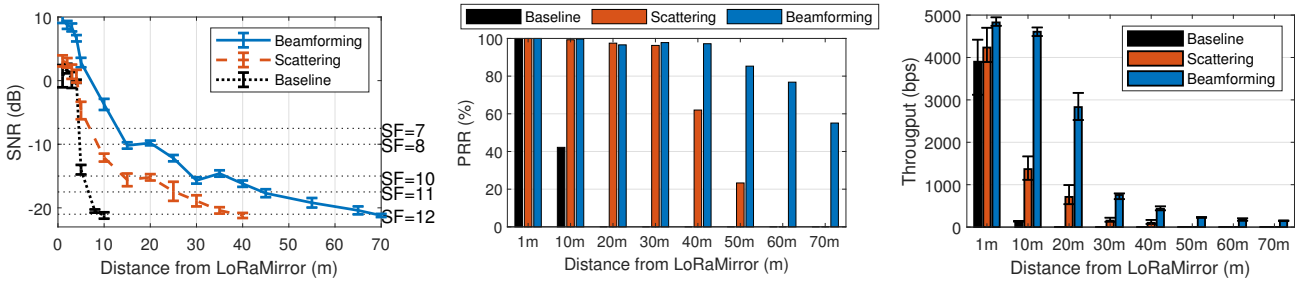

(a) SNR (b) PRR (SF=12) (b) Throughput

Fig. 17. Communication improvement of LoRaMirror over distances. The baseline is the case without LoRaMirror.

and achieves the *global* optimal. Since the brute-force search takes unacceptable amount of time for fully exploring the configuration space of the 16-antenna prototype (around 50 days with LoRa's fastest data rate), we test with only half of antenna elements (8 elements) in this experiment. The same experimental setup is applied during the SNR measurement for both search schemes.

Fig. 16(a) plots the CDF of their SNR differences, which suggests that the LoRaMirror beam search scheme is able to achieve near optimal performance with 50-percentile gap of 0.3 dB and 90-percentile gap of 0.7 dB. The results indeed suggest high efficacy of the proposed beam search scheme.

Fig. 16(b) plots one instance of the measured SNR performance over different LoRaMirror configurations. The result shows that the LoRaMirror beam search completes the search process within 2 s (at SF12 in this instance), which is significantly shorter than the ∼1200 s of the global optimal search. The highest SNR achieved by the LoRaMirror beam search is -19.3 dB, which is very close to the -18.9 dB achieved by the global optimal.

D. Communication Improvement

We evaluate the communication improvement in terms of SNR, PRR and throughput for blind-spot nodes of varied distances from the LoRaMirror. We measure the results with LoRaMirror (beamforming or scattering) and without LoRaMirror (baseline), respectively.

Fig. 17(a) presents the SNR results. The received SNR with the baseline decreases dramatically when the node moves only 5 m away from LoRaMirror mainly due to the loss of LOS signal path. The blind spot appears after 10 m, where the average SNR of baseline is below -22 dB. With the SNR gain, LoRaMirror in the beamforming mode can achieve nearly 70 m extension of the communication range into the blind-spot region. With scattering mode, LoRaMirror can still achieve 40 m range extension. Fig. 17(a) also marks down the required SNR conditions for demodulation with different SF settings [59].

Fig. 17(b) plots the achieved PRR over the distance. PRR is measured as the correctly demodulated packets over the total number of transmitted (1000 packets with SF12 from the end node). The LoRa communication is considered robust when the PRR is higher than 80%. The baseline achieves the robust communication within 5 m only, while LoRaMirror can extend the robust communication by 50 m into the blind-spot region (in beamforming mode). It goes as far as 70 m and still achieves near 60% PRR.

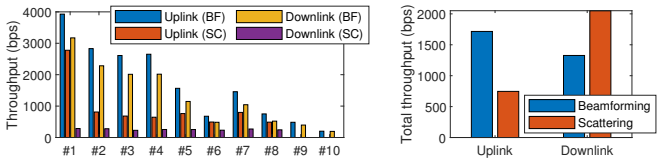

(a) (b)

Fig. 18. (a) Achieved throughput of individual end nodes with beamforming (BF) and scattering (SC). (b) Overall network throughput.

Fig. 17(c) plots the achieved throughput. Standard adaptive data rate (ADR) scheme as advised by LoRaWAN is implemented based on its open source project [60] so the end nodes adaptively select appropriate SF according to the SNR conditions. From the results, beamforming generally achieves higher throughput than scattering does, mainly due to its higher SNR gain and thus more opportunities for faster SF settings with ADR. We observe decreased throughput when the node moves away from LoRaMirror due to SNR drops. In all cases, both beamforming and scattering mode achieve high throughput gain on top of the baseline.

E. Multiple Blind-Spot Nodes

To examine the performance gain with multiple end nodes, we experiment with ten LoRa nodes deployed within the blind-spot region (#1∼#10 denote 5m, 10m, 15m, 20m, 25m, 30m, 35m, 40m, 50m and 60m away from LoRaMirror). We evaluate the throughput by measuring the time cost to deliver the same amount of data successfully on the uplink and downlink, respectively. Fig. 18(a) plots the measured throughput of individual nodes. The achieved throughput varies with different node locations due to their SNR conditions. During the experiment, node #9 and #10 (50 m and 60 m away from LoRaMirror) are not reachable in the scattering mode, but can still be reached by beamforming. Fig. 18(b) reports the overall network throughput. We discuss the results of the uplink and downlink separately.

On the uplink, TDMA is applied to coordinate the multiple end nodes for both beamforming and scattering. We observe that the network throughput in the beamforming mode is 1.7× higher than that of the scattering mode. This is reasonable as

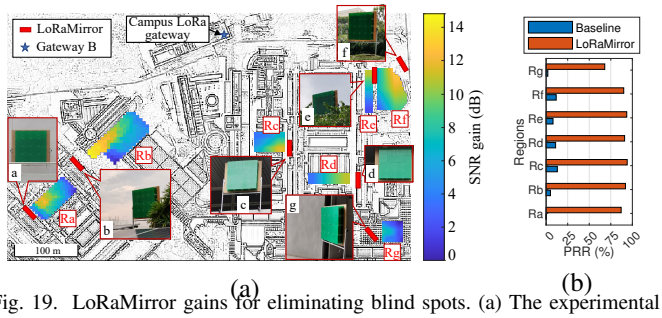

Fig. 19. LoRaMirror gains for eliminating blind spots. (a) The experimental setting with annotated blind-spot regions, LoRaMirror deployment, and SNR gains across the seven regions. (b) The PRR gains across the seven regions.

beamforming provides a higher SNR gain on the uplinks of individual end nodes.

On the downlink, however, the scattering mode achieves 1.5× throughput compared with the beamforming mode because it allows the gateway to multicast the command packets in a one-to-many style (SF12 is chosen for broadcasting to ensure delivery). On the other hand, the beamforming mode only supports separately delivering the same packet to different end nodes by one-to-one transmissions (though with the best beamforming configurations and SFs). The network throughput in scattering mode is the sum of each node's throughput (2051 bps), while the beamforming mode has an average network throughput of 1327 bps across all nodes.

VIII. Application Study

We study real world applications of LoRaMirror and evaluate the gain from its usage. We perform experiments with the second testbed as depicted in Fig. 1, which involves real and more diversified application conditions with different landscapes, indoor/outdoor scenarios and various types of signal blockage. The application study considers two typical cases of LoRaMirror usage, *i.e.*, (i) when deployed near the blind spot region to eliminate the blind spots, (ii) when deployed near the gateway side for generally enhancing the communication including non-blind spot nodes.

A. Eliminating Blind Spots

We deploy LoRaMirror near each of the seven blind-spot regions as highlighted in Fig. 1 to eliminate blind spots. The original SNR conditions are below -22 dB in all seven regions. As annotated in Fig. 19(a), those blind-spot regions mainly feature low-lying land (region 'Ra', 'Rb', 'Re', 'Rf'), regions behind building blockage (region 'Ra', 'Rc', 'Rd'), or indoor environment (region 'Rf', 'Rg'). LoRaMirror can be best deployed at various locations to support different regions. We conduct experiments to evaluate the beamforming mode of LoRaMirror in terms of SNR and PRR gains as reported in Fig. 19. We discuss the results as follows.

- With the deployment of LoRaMirror, the SNR is improved on average by 7.8 dB for the seven regions (Fig. 19(a)), and the PRR is improved from lower than 10% for most regions to more than 85% for most regions as presented in Fig. 19(b). The LoRa gateway has high sensitivity (*i.e.*, -137 dBm), meaning that even a small SNR gain may lead to vital improvement of the link PRR.
- According to the heatmap of SNR gains in Fig. 19(a), we observe higher SNR gains when the node is closer to the deployed LoRaMirror. This is expected as the shorter distance between the node and LoRaMirror leads to better SNR controllability.

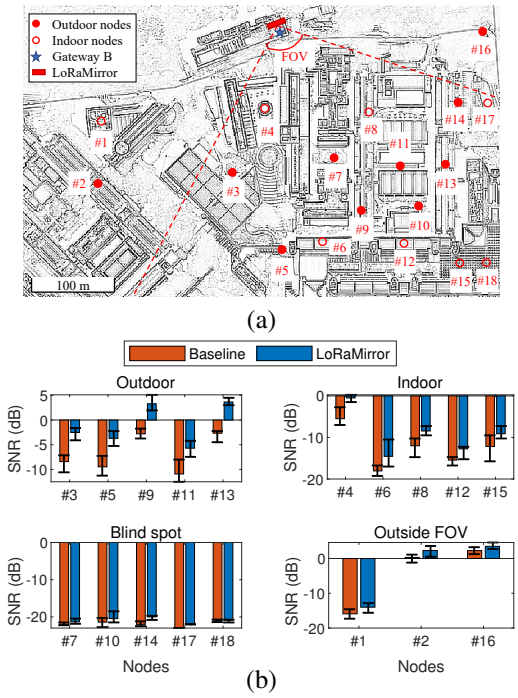

Fig. 20. LoRaMirror gains for general communication enhancement. (a) The experimental setting with annotated LoRaMirror deployment and locations of testing nodes. (b) The SNR gains across different types of testing nodes.

B. Enhancing General Communication

We deploy LoRaMirror near the gateway side to enhance general communication quality. As annotated in Fig. 20(a), eighteen end nodes distributed in the field comprise four types of cases for evaluation, namely indoor (node #1, #4, #6, #8, #12, #15 and #17-18), outdoor (node #2, #3, #5, #7, #9-11, #13-14 and #16), blind spot (node #7, #10, #14 and #17-18) and outside FOV (node #1-2 and #16). Fig. 20(b) plots SNR of those nodes. We discuss the results as follows.

- Outdoor nodes gain the highest (5.9 dB on average) from LoRaMirror enhancement, among which the SNR gains of node #9 and #13 are higher than the rest (#3, #5, #11 and so on) mainly because #9 and #13 are placed on the rooftops with LOS to the gateway, whereas the rest do not have LOS.
- Indoor nodes typically have lower gains (3.5 dB on average), which is expected as they usually do not have direct path to the gateway so the signal strength after LoRaMirror reflection is not high. Node #4 is the only exception since it is close to the gateway and LoRaMirror.
- Blind-spot nodes generally gain very little, mainly due to the fact that LoRaMirror at the gateway side cannot provide additional LOS to those blind spots, which is different from the case when we deploy LoRaMirror near the blind-spot regions.

TABLE I
COMPARISON BETWEEN LORAMIRROR AND ADDITIONAL LORA GATEWAY

Aspect	LoRaMirror	Additional LoRa Gateway
Device Cost	˜$50–$100 per unit (large-scale manufacturing)	˜$300–$500 per unit (complete outdoor gateway, e.g., RAK7249)
Deployment Cost	Minimal – requires mounting on a pole/roof, no cabling required (**battery-powered**)	High – requires mounting on a pole/roof, plus power & network cabling
Maintenance Cost	Low – occasional battery replacement (every 3–5 years)	Moderate – ongoing power/network checks (every year)
Coverage Range	Localized improvement – covers tens to a few hundred meters (**fills blind spots**)	Wide-area coverage – typically 1–3 km in urban settings
Deployment Flexibility	High – can be installed almost anywhere without infrastructure constraints	Limited – needs accessible power and network connectivity
Primary Use-case	Complementary tool for addressing specific blind spots in existing coverage	Backbone to expand overall network coverage and add capacity

Even that, we see node #10 and #14 become reachable with such little SNR gains – the PRR improved from 11% to 63% for node #10 and 8% to 51% for node #14.

• Surprisingly, LoRaMirror also has gains (1.7 dB on average) to the nodes outside the FOV (#1, #2 and #16). This is because the beamforming search can choose a better path to communicate with those nodes through ambient reflection.

IX. DISCUSSION

A. Cost Comparison

Table I provides a detailed cost comparison between LoRaMirror and the addition of more gateways. LoRaMirror and additional gateways are not mutually exclusive but complementary solutions in a LoRa network. Each is suitable for different scenarios: LoRaMirror is ideal for addressing specific blind spots caused by complex urban geometry when general coverage already exists from existing gateways. Instead of installing another full gateway, which would largely duplicate existing coverage, LoRaMirror provides a targeted, efficient solution. The cost of LoRaMirror can be categorized as follows:

(i) Device Cost: LoRaMirror utilizes PCB-based antennas operating in the sub-GHz (915 MHz) band, using cost-effective materials (e.g., FR4) without significantly compromising RF performance. With large-scale manufacturing, fixed PCB production costs such as equipment setup, tooling, and process development are distributed across numerous units. The backscatter circuitry typically incurs negligible costs, similar to RFID tags [61]–[64]. For digital components, LoRa chipsets (e.g., SX127x or SX126x series) range between $6-$9 per unit. Given LoRa's low data rate (<10 kbps), cost-efficient MCUs like the STM32 or MSP430 series, priced approximately $1-$4 per unit, are suitable. Overall, the total device cost of LoRaMirror is projected between $50-$100, notably lower than commercial LoRa gateways such as RAK7249.

(ii) Deployment Cost: Both LoRaMirror and LoRa gateways require pole or rooftop installation. However, LoRaMirror can operate for several years on battery power, eliminating the need for cabling work related to power and network connectivity.

(iii) Maintenance Cost: Powered by batteries, LoRaMirror requires battery replacement every 3–5 years. In contrast, outdoor LoRa gateways, typically powered by mains electricity (e.g., 220 V), necessitate regular inspections and cable maintenance at least annually.

In summary, LoRaMirror offers a targeted, cost-effective, and flexible approach to resolving specific coverage gaps with minimal installation and maintenance requirements. Deploying additional gateways, while offering broader coverage, entails higher initial investment and ongoing costs, making gateways more suitable for extensive network expansions rather than isolated blind spot mitigation.

B. Capacity of LoRaMirror

LoRaMirror works at the physical layer by creating an additional reflection path, which strengthens the wireless channel for LoRa nodes trapped in blind spots. In theory, therefore, a single LoRaMirror will not outperform the intrinsic capacity of the LoRa physical layer itself. In practice, two factors set the real-world limit:

Reflection gain. Our current prototype improves signal penetration by as much as 70 m into a blind-spot region. A higher reflection gain would enlarge the effective coverage area and, in turn, cover more blind-spot nodes within range.

TDMA scheduling. LoRaMirror schedules the blind-spot nodes in a time-division manner. As the number of served nodes grows, each node receives a narrower transmission window, placing stricter demands on the TDMA scheme and on MAC-layer efficiency.

Designing more powerful meta-surfaces and developing a lightweight MAC that scales to many nodes are promising directions we will pursue in future work.

C. Concurrent LoRa Transmissions

When LoRaMirror employs beamforming to serve multiple LoRa nodes, it utilizes TDMA to schedule individual transmissions from each blind-spot node, which does not support concurrent transmissions.

When LoRaMirror uses the scattering mode to serve multiple LoRa nodes, concurrent transmission can be supported. The scattering mode of LoRaMirror has a 2.7x wider beam than beamforming at the expense of the 5.8dB peak gain, thus covering more nodes in different directions at the same time.

If all the nodes are covered by the beam of the scattering mode, LoRaMirror will not be affected by the concurrent transmissions. This is because LoRaMirror works at the physical layer to provide a wireless channel for LoRa communication.

The concurrent transmission is handled by LoRa communication capacity, which is orthogonal to LoRaMirror.

If some nodes are outside the beam coverage of the scattering mode, LoRaMirror may not be able to assist the concurrent transmissions for these nodes, as the reflection beam cannot reach the nodes in the scattering mode.

X. Conclusion and Future Work

This paper presents LoRaMirror, the first reflective smart surface solution designed to eliminate blind spots and enhance communication quality in urban LPWAN deployments. LoRaMirror addresses three key challenges unique to LPWAN applications: (1) to mitigate reflection loss over kilometer-scale distances, it adopts a polarization-agnostic, high-gain antenna design with co-designed phase shifters; (2) to overcome the prohibitive overhead of beam search under ultra-low data rates, it introduces a blind beamforming scheme with symbol-level probing; and (3) to support wide-area coverage, it enables a scattering mode that broadens the beam direction range without requiring prior node location knowledge. Extensive experiments validate the design's effectiveness in real-world scenarios. Future work may explore efficient MAC layer designs for multi-user access and coordinated deployment strategies involving multiple smart surfaces.

References

[1] L. Alliance, "Lorawan specification," https://lora-alliance.org/about-lorawan/, 2023, accessed: 2023-02-08.

[2] V. A. L. Sobral, N. Saoda, R. Shah, W. Wang, and B. Campbell, "Retroiot: Retrofitting internet of things deployments by hiding data in battery readings," in *Proceedings of the 28th Annual International Conference on Mobile Computing And Networking*, ser. MobiCom '22. New York, NY, USA: Association for Computing Machinery, 2022, pp. 69–81. [Online]. Available: https://doi.org/10.1145/3495243.3560536

[3] GSMA, "Narrowband - internet of things (nb-iot)," https://www.gsma.com/iot/narrow-band-internet-of-things-nb-iot/, 2023, accessed: 2023-02-08.

[4] W. Xu, J. Y. Kim, W. Huang, S. S. Kanhere, S. K. Jha, and W. Hu, "Measurement, characterization, and modeling of lora technology in multifloor buildings," *IEEE Internet of Things Journal*, vol. 7, no. 1, pp. 298–310, 2020.

[5] S. Tong, J. Wang, J. Yang, Y. Liu, and J. Zhang, "Citywide lora network deployment and operation: Measurements, analysis, and implications," in *Proceedings of the 21st ACM Conference on Embedded Networked Sensor Systems*, ser. SenSys '23. New York, NY, USA: Association for Computing Machinery, 2024, pp. 362–375. [Online]. Available: https://doi.org/10.1145/3625687.3625796

[6] E. Lumet, A. Le Floch, R. Kacimi, M. Lihoreau, and A.-L. Beylot, "Lorawan relaying: Push the cell boundaries," in *Proceedings of the 24th International ACM Conference on Modeling, Analysis and Simulation of Wireless and Mobile Systems*, 2021, pp. 217–220.

[7] O. Flauzac, J. Herard, F. Nolot, and P. Cola, "A low power lora-lorawan relay function with a single input, single output device," in *Proceedings of the 2020 International Conference on Embedded Wireless Systems and Networks on Proceedings of the 2020 International Conference on Embedded Wireless Systems and Networks*, ser. EWSN '20. USA: Junction Publishing, 2020, pp. 283–288.

[8] R. Eletreby, D. Zhang, S. Kumar, and O. Yağan, "Empowering low-power wide area networks in urban settings," in *Proceedings of the Conference of the ACM Special Interest Group on Data Communication*, ser. SIGCOMM '17. New York, NY, USA: Association for Computing Machinery, 2017, pp. 309–321. [Online]. Available: https://doi.org/10.1145/3098822.3098845

[9] S. Tong, Z. Shen, Y. Liu, and J. Wang, "Combating link dynamics for reliable lora connection in urban settings," in *Proceedings of the 27th Annual International Conference on Mobile Computing and Networking*, ser. MobiCom '21. New York, NY, USA: Association for Computing Machinery, 2021, pp. 642–655. [Online]. Available: https://doi.org/10.1145/3447993.3483250

[10] C. Li, H. Guo, S. Tong, X. Zeng, Z. Cao, M. Zhang, Q. Yan, L. Xiao, J. Wang, and Y. Liu, "Nelora: Towards ultra-low snr lora communication with neural-enhanced demodulation," in *Proceedings of the 19th ACM Conference on Embedded Networked Sensor Systems*, ser. SenSys '21. New York, NY, USA: Association for Computing Machinery, 2021, pp. 56–68. [Online]. Available: https://doi.org/10.1145/3485730.3485928

[11] A. Dongare, R. Narayanan, A. Gadre, A. Luong, A. Balanuta, S. Kumar, B. Iannucci, and A. Rowe, "Charm: Exploiting geographical diversity through coherent combining in low-power wide-area networks," in *2018 17th ACM/IEEE International Conference on Information Processing in Sensor Networks (IPSN)*, 2018, pp. 60–71.

[12] J. Liu, W. Xu, S. Jha, and W. Hu, "Nephalai: Towards lpwan c-ran with physical layer compression," in *Proceedings of the 26th Annual International Conference on Mobile Computing and Networking*, ser. MobiCom '20. New York, NY, USA: Association for Computing Machinery, 2020. [Online]. Available: https://doi.org/10.1145/3372224.3419193

[13] A. Balanuta, N. Pereira, S. Kumar, and A. Rowe, "A cloud-optimized link layer for low-power wide-area networks," in *Proceedings of the 18th International Conference on Mobile Systems, Applications, and Services*, ser. MobiSys '20. New York, NY, USA: Association for Computing Machinery, 2020, pp. 247–259. [Online]. Available: https://doi.org/10.1145/3386901.3388915

[14] A. Gadre, R. Narayanan, A. Luong, A. Rowe, B. Iannucci, and S. Kumar, "Frequency configuration for Low-Power Wide-Area networks in a heartbeat," in *17th USENIX Symposium on Networked Systems Design and Implementation (NSDI 20)*. Santa Clara, CA: USENIX Association, Feb. 2020, pp. 339–352. [Online]. Available: https://www.usenix.org/conference/nsdi20/presentation/gadre

[15] X. Zhou, Z. Zhang, Y. Zhu, Y. Li, S. Kumar, A. Vahdat, B. Y. Zhao, and H. Zheng, "Mirror mirror on the ceiling: Flexible wireless links for data centers," in *Proceedings of the ACM SIGCOMM 2012 Conference on Applications, Technologies, Architectures, and Protocols for Computer Communication*, ser. SIGCOMM '12. New York, NY, USA: Association for Computing Machinery, 2012, pp. 443–454. [Online]. Available: https://doi.org/10.1145/2342356.2342440

[16] K. Qian, L. Yao, X. Zhang, and T. N. Ng, "Millimirror: 3d printed reflecting surface for millimeter-wave coverage expansion," in *Proceedings of ACM MobiCom*, 2022.

[17] Z. Peng, L. Li, M. Wang, Z. Zhang, Q. Liu, Y. Liu, and R. Liu, "An effective coverage scheme with passive-reflectors for urban millimeter-wave communication," *IEEE Antennas and Wireless Propagation Letters*, vol. 15, pp. 398–401, 2016.

[18] Z. Li, Y. Xie, L. Shangguan, R. I. Zelaya, J. Gummeson, W. Hu, and K. Jamieson, "Towards programming the radio environment with large arrays of inexpensive antennas," in *16th USENIX Symposium on Networked Systems Design and Implementation (NSDI 19)*. Boston, MA: USENIX Association, Feb. 2019, pp. 285–300. [Online]. Available: https://www.usenix.org/conference/nsdi19/presentation/lizhuqi

[19] M. Dunna, C. Zhang, D. Sievenpiper, and D. Bharadia, "Scattermimo: Enabling virtual mimo with smart surfaces," in *Proceedings of the 26th Annual International Conference on Mobile Computing and Networking*, ser. MobiCom '20. New York, NY, USA: Association for Computing Machinery, 2020. [Online]. Available: https://doi.org/10.1145/3372224.3380887

[20] V. Arun and H. Balakrishnan, "Rfocus: Beamforming using thousands of passive antennas," in *17th USENIX Symposium on Networked Systems Design and Implementation (NSDI 20)*. Santa Clara, CA: USENIX Association, Feb. 2020, pp. 1047–1061. [Online]. Available: https://www.usenix.org/conference/nsdi20/presentation/arun

[21] C. Feng, X. Li, Y. Zhang, X. Wang, L. Chang, F. Wang, X. Zhang, and X. Chen, "Rflens: Metasurface-enabled beamforming for iot communication and sensing," in *Proceedings of the 27th Annual International Conference on Mobile Computing and Networking*, ser. MobiCom '21. New York, NY, USA: Association for Computing Machinery, 2021, pp. 587–600. [Online]. Available: https://doi.org/10.1145/3447993.3483238

[22] K. Cho, M. Mazaheri, J. Gummeson, O. Abari, and K. Jamieson, "A steerable, transflective metamaterial surface for nextg mmwave networks," in *20th USENIX Symposium on Networked Systems Design and Implementation (NSDI 23)*. Boston, MA: USENIX Association, Apr. 2023.

[23] I. K. Jain, R. Subbaraman, and D. Bharadia, "Two beams are better than one: Towards reliable and high throughput mmwave links," in *Proceedings of the 2021 ACM SIGCOMM 2021 Conference*, ser. SIGCOMM '21. New York, NY, USA: Association for

Computing Machinery, 2021, pp. 488–502. [Online]. Available: https://doi.org/10.1145/3452296.3472924

[24] R. I. Zelaya, W. Sussman, J. Gummeson, K. Jamieson, and W. Hu, "Lava: Fine-grained 3d indoor wireless coverage for small iot devices," in *Proceedings of the 2021 ACM SIGCOMM 2021 Conference*, ser. SIGCOMM '21. New York, NY, USA: Association for Computing Machinery, 2021, pp. 123–136. [Online]. Available: https://doi.org/10.1145/3452296.3472890

[25] K. W. Cho, M. H. Mazaheri, J. Gummeson, O. Abari, and K. Jamieson, "Mmwall: A reconfigurable metamaterial surface for mmwave networks," in *Proceedings of the 22nd International Workshop on Mobile Computing Systems and Applications*, ser. HotMobile '21. New York, NY, USA: Association for Computing Machinery, 2021, pp. 119–125. [Online]. Available: https://doi.org/10.1145/3446382.3448665

[26] R. I. Zelaya, R. Ma, and W. Hu, "Towards 6g and beyond: Smarten everything with metamorphic surfaces," in *Proceedings of the Twentieth ACM Workshop on Hot Topics in Networks*, ser. HotNets '21. New York, NY, USA: Association for Computing Machinery, 2021, pp. 155–162. [Online]. Available: https://doi.org/10.1145/3484266.3487385

[27] C. Liaskos, A. Tsioliaridou, S. Nie, A. Pitsillides, S. Ioannidis, and I. F. Akyildiz, "On the network-layer modeling and configuration of programmable wireless environments," *IEEE/ACM transactions on networking*, vol. 27, no. 4, pp. 1696–1713, 2019.

[28] C. Liaskos, L. Mamatas, A. Pourdamghani, A. Tsioliaridou, S. Ioannidis, A. Pitsillides, S. Schmid, and I. F. Akyildiz, "Software-defined reconfigurable intelligent surfaces: From theory to end-to-end implementation," *Proceedings of the IEEE*, 2022.

[29] J. Nolan, K. Qian, and X. Zhang, "Ros: Passive smart surface for roadside-to-vehicle communication," in *Proceedings of the 2021 ACM SIGCOMM 2021 Conference*, ser. SIGCOMM '21. New York, NY, USA: Association for Computing Machinery, 2021, pp. 165–178. [Online]. Available: https://doi.org/10.1145/3452296.3472896

[30] F. Liu, O. Tsilipakos, A. Pitilakis, A. C. Tasolamprou, M. S. Mirmoosa, N. V. Kantartzis, D.-H. Kwon, J. Georgiou, K. Kossifos, M. A. Antoniades *et al.*, "Intelligent metasurfaces with continuously tunable local surface impedance for multiple reconfigurable functions," *Physical Review Applied*, vol. 11, no. 4, p. 044024, 2019.

[31] G. Lan, M. F. Imani, Z. Liu, J. Manjarrés, W. Hu, A. S. Lan, D. R. Smith, and M. Gorlatova, "Metasense: Boosting rf sensing accuracy using dynamic metasurface antenna," *IEEE Internet of Things Journal*, vol. 8, no. 18, pp. 14 110–14 126, 2021.

[32] A. Pallaprolu, W. Hurst, S. Paul, and Y. Mostofi, *I Beg to Diffract: RF Field Programming With Edges*. New York, NY, USA: Association for Computing Machinery, 2023. [Online]. Available: https://doi.org/10.1145/3570361.3613266

[33] H. Pan, L. Qiu, B. Ouyang, S. Zheng, Y. Zhang, Y.-C. Chen, and G. Xue, *PMSat: Optimizing Passive Metasurface for Low Earth Orbit Satellite Communication*. New York, NY, USA: Association for Computing Machinery, 2023. [Online]. Available: https://doi.org/10.1145/3570361.3613257

[34] Y. Zhang, Y. Wang, L. Yang, M. Wang, Y.-C. Chen, L. Qiu, Y. Liu, G. Xue, and J. Yu, "Acoustic sensing and communication using metasurface," in *20th USENIX Symposium on Networked Systems Design and Implementation (NSDI 23)*. Boston, MA: USENIX Association, Apr. 2023, pp. 1359–1374. [Online]. Available: https://www.usenix.org/conference/nsdi23/presentation/zhang-yongzhao

[35] L. Chen, W. Hu, K. Jamieson, X. Chen, D. Fang, and J. Gummeson, "Pushing the physical limits of iot devices with programmable metasurfaces," in *18th USENIX Symposium on Networked Systems Design and Implementation (NSDI 21)*. USENIX Association, Apr. 2021, pp. 425–438. [Online]. Available: https://www.usenix.org/conference/nsdi21/presentation/chen

[36] X. Li, C. Feng, X. Wang, Y. Zhang, Y. Xie, and X. Chen, "RF-Bouncer: A programmable dual-band metasurface for sub-6 wireless networks," in *20th USENIX Symposium on Networked Systems Design and Implementation (NSDI 23)*. Boston, MA: USENIX Association, Apr. 2023, pp. 389–404. [Online]. Available: https://www.usenix.org/conference/nsdi23/presentation/li-xinyi

[37] R. Ma, R. I. Zelaya, and W. Hu, *Softly, Deftly, Scrolls Unfurl Their Splendor: Rolling Flexible Surfaces for Wideband Wireless*. New York, NY, USA: Association for Computing Machinery, 2023. [Online]. Available: https://doi.org/10.1145/3570361.3592520

[38] O. García-Pérez, F. Tercero, I. Malo, J. Gallego, and J. López-Pérez, "Linear to circular polarization conversion using microwave hybrids for brand (1.5-15.5 ghz)," *CDT Technical Report 2018-12*, 2018.

[39] J. Lietzen, A. Liljemark, R. Duan, R. Jäntti, and V. Viikari, "Polarization conversion-based ambient backscatter system," *IEEE Access*, vol. 8, pp. 216 793–216 804, 2020.

[40] H. Zhu, S. Cheung, K. L. Chung, and T. I. Yuk, "Linear-to-circular polarization conversion using metasurface," *IEEE transactions on antennas and propagation*, vol. 61, no. 9, pp. 4615–4623, 2013.

[41] R. Orr, G. Goussetis, V. Fusco, and E. Saenz, "Linear-to-circular polarization reflector with transmission band," *IEEE Transactions on Antennas and Propagation*, vol. 63, no. 5, pp. 1949–1956, 2015.

[42] P. Naseri, G. Goussetis, N. J. Fonseca, and S. V. Hum, "Synthesis of multi-band reflective polarizing metasurfaces using a generative adversarial network," *Scientific Reports*, vol. 12, no. 1, p. 17006, 2022.

[43] J.-L. Wu, B.-Q. Lin, X.-Y. Da, and K. Wu, "A linear-to-circular polarization converter based on i-shaped circular frequency selective surfaces," *Chinese Physics B*, vol. 26, no. 9, p. 094201, 2017.

[44] O. Abari, D. Bharadia, A. Duffield, and D. Katabi, "Enabling High-Quality untethered virtual reality," in *14th USENIX Symposium on Networked Systems Design and Implementation (NSDI 17)*. Boston, MA: USENIX Association, Mar. 2017, pp. 531–544. [Online]. Available: https://www.usenix.org/conference/nsdi17/technical-sessions/presentation/abari

[45] X. Zhang, W. Xu, G. Cai, Y. Song, and G. Chen, "A new reconfigurable intelligent-surface-assisted lora system," *IEEE Transactions on Vehicular Technology*, vol. 71, no. 8, pp. 9055–9060, 2022.

[46] Z. Liang, G. Cai, J. He, G. Kaddoum, C. Huang, and M. Debbah, "Ris-enabled anti-interference in lora systems," *IEEE Transactions on Communications*, vol. 72, no. 10, pp. 6599–6616, 2024.

[47] B. Kellogg, V. Talla, S. Gollakota, and J. R. Smith, "Passive wi-fi: Bringing low power to wi-fi transmissions," in *Proceedings of the 13th Usenix Conference on Networked Systems Design and Implementation*, ser. NSDI'16. USA: USENIX Association, 2016, pp. 151–164.

[48] A. Ramos, T. Varum, and J. N. Matos, "Compact multilayer yagi-uda based antenna for iot/5g sensors," *Sensors*, vol. 18, no. 9, 2018. [Online]. Available: https://www.mdpi.com/1424-8220/18/9/2914

[49] O. Kramer, T. Djerafi, and K. Wu, "Vertically multilayer-stacked yagi antenna with single and dual polarizations," *IEEE Transactions on Antennas and Propagation*, vol. 58, no. 4, pp. 1022–1030, 2010.

[50] R. C. Johnson, H. A. Ecker, and J. S. Hollis, "Determination of far-field antenna patterns from near-field measurements," *Proceedings of the IEEE*, vol. 61, no. 12, pp. 1668–1694, 1973.

[51] P. Delos, B. Broughton, and J. Kraft, "Phased array antenna patterns-part 1: Linear array beam characteristics and array factor," *Analog Dialogue*, vol. 54, pp. 1–3, 2020.

[52] C. A. Balanis, *Antenna theory: analysis and design*. John wiley & sons, 2015.

[53] A. Gamage, J. C. Liando, C. Gu, R. Tan, and M. Li, "Lmac: Efficient carrier-sense multiple access for lora," in *Proceedings of the 26th Annual International Conference on Mobile Computing and Networking*, ser. MobiCom '20. New York, NY, USA: Association for Computing Machinery, 2020. [Online]. Available: https://doi.org/10.1145/3372224.3419200

[54] Semtech, "Sx1276 lora core 137mhz to 1020mhz long range low power transceiver," https://www.semtech.com/products/wireless-rf/lora-connect/sx1276, Rev. 7, 2020.

[55] R. Subbaraman, Y. Guntupalli, S. Jain, R. Kumar, K. Chintalapudi, and D. Bharadia, "Bsma: Scalable lora networks using full duplex gateways," in *Proceedings of the 28th Annual International Conference on Mobile Computing And Networking*, ser. MobiCom '22. New York, NY, USA: Association for Computing Machinery, 2022, pp. 676–689. [Online]. Available: https://doi.org/10.1145/3495243.3560544

[56] E. Liri, K. Ramakrishnan, and K. Koushik, "A renewable energy-aware distributed task scheduler for multi-sensor iot networks," in *Proceedings of the ACM SIGCOMM Workshop on Networked Sensing Systems for a Sustainable Society*, 2022, pp. 26–32.

[57] M. Vigil-Hayes, M. N. Hossain, A. K. Elliott, E. M. Belding, and E. Zegura, "Lorax: Repurposing lora as a low data rate messaging system to extend internet boundaries," in *ACM SIGCAS/SIGCHI Conference on Computing and Sustainable Societies (COMPASS)*, 2022, pp. 195–213.

[58] T. Instruments, "Msp430fr5969 datasheet," http://www.ti.com/lit/ds/symlink/msp430fr5969.pdf, 2018.

[59] J. C. Liando, A. Gamage, A. W. Tengourtius, and M. Li, "Known and unknown facts of lora: Experiences from a large-scale measurement study," *ACM Trans. Sen. Netw.*, vol. 15, no. 2, feb 2019. [Online]. Available: https://doi.org/10.1145/3293534

[60] L. Alliance, "Implementing adaptive data rate (adr)," https://lora-developers.semtech.com/documentation/tech-papers-and-guides/

implementing-adaptive-data-rate-adr/implementing-adaptive-data-rate/, 2022, accessed: 2022-09-05.

[61] S. Li, C. Zhang, Y. Song, H. Zheng, L. Liu, L. Lu, and M. Li, "Internet-of-microchips: Direct radio-to-bus communication with spi backscatter," in *The 26th Annual International Conference on Mobile Computing and Networking*, ser. MobiCom '20. London, United Kingdom: Association for Computing Machinery, 2020.

[62] S. Li, Q. Meng, Y. Bai, C. Zhang, Y. Song, S. Li, and L. Lu, "Go beyond rfid: Rethinking the design of rfid sensor tags for versatile applications," in *Proceedings of the 29th Annual International Conference on Mobile Computing and Networking*, ser. ACM MobiCom '23. New York, NY, USA: Association for Computing Machinery, 2023. [Online]. Available: https://doi.org/10.1145/3570361.3613284

[63] S. Li, S. Li, M. Chen, C. Song, and L. Lu, "Frequency scaling meets intermittency: Optimizing task rate for rfid-scale computing devices," *IEEE Transactions on Mobile Computing*, vol. 23, no. 2, pp. 1689–1700, 2024.

[64] S. Li, H. Zheng, C. Zhang, Y. Song, S. Yang, M. Chen, L. Lu, and M. Li, "Passive DSSS: Empowering the downlink communication for backscatter systems," in *19th USENIX Symposium on Networked Systems Design and Implementation (NSDI 22)*. Renton, WA: USENIX Association, Apr. 2022, pp. 913–928. [Online]. Available: https://www.usenix.org/conference/nsdi22/presentation/li-songfan

[65] A. Theory, "Rectangular patch antenna design," https://www.antenna-theory.com/antennas/patches/antenna.php, 2022, accessed: 2022-09-05.